





RESEARCH ARTICLE | JUNE 04 2024

Void closure in a pulsed complex plasma in microgravity

C. A. Knapek   ; D. P. Mohr  ; P. Huber 



Phys. Plasmas 31, 063702 (2024)

<https://doi.org/10.1063/5.0204998>



01 July 2024 10:17:30

AIP Advances

Why Publish With Us?

-  **25 DAYS**
average time to 1st decision
-  **740+ DOWNLOADS**
average per article
-  **INCLUSIVE**
scope

[Learn More](#)

Void closure in a pulsed complex plasma in microgravity

Cite as: Phys. Plasmas **31**, 063702 (2024); doi: 10.1063/5.0204998

Submitted: 23 February 2024 · Accepted: 19 May 2024 ·

Published Online: 4 June 2024



View Online



Export Citation



CrossMark

C. A. Knapik,^{1,2,a)}  D. P. Mohr,^{1,2}  and P. Huber² 

AFFILIATIONS

¹Institute of Physics, University of Greifswald, 17489 Greifswald, Germany

²Institut für Materialphysik im Weltraum, Deutsches Zentrum für Luft- und Raumfahrt, 51147 Köln, Germany

^{a)} Author to whom correspondence should be addressed: christina.knapik@physik.uni-greifswald.de

ABSTRACT

A new experimental method for creating void-free complex (dusty) plasmas under microgravity conditions is presented. The method is based on a pulsed operation mode of a four-channel radio frequency generator for plasma sustainment. A dust cloud of micrometer-sized particles can be immersed in the bulk of a low temperature plasma under microgravity conditions. It typically contains a central volume depleted of particles—the void—that prevents the generation of large, continuous clouds. Experiments performed at different neutral gas pressures and discharge volumes during the microgravity phase of a parabolic flight show that the central void is closed completely once the pulsed operation mode is applied. The particle cloud shape and the density distribution within the cloud are practically independent of the pulse period within the investigated parameter range and mainly depend on the overall discharge parameters neutral gas pressure and discharge volume. This indicates that the pulsed operation of the plasma source does not introduce new physical effects on the particles aside from the void closure. The proposed method has great potential for future application in experimental facilities dedicated to fundamental studies of large three-dimensional, homogeneous complex plasma systems in microgravity.

© 2024 Author(s). All article content, except where otherwise noted, is licensed under a Creative Commons Attribution (CC BY) license (<https://creativecommons.org/licenses/by/4.0/>). <https://doi.org/10.1063/5.0204998>

I. INTRODUCTION

Laboratory complex plasmas are low-temperature plasmas containing nano- to micrometer sized particles as an additional component.^{1–4} In the plasma, the particles acquire negative charges up to several thousands of elementary charges, with the charge mainly depending on the particle size and the electron temperature T_e of the plasma. The particles interact via a screened Coulomb potential and form strongly coupled many-particles systems in a variety of states (solid, liquid, and gaseous).

The particles are individually observable by optical diagnostics, and fundamental processes of many-particle physics can be studied, e.g., phase transitions,^{5,6} nonlinear waves,^{7–9} or turbulence.^{10,11}

Gravity forces the particles to sediment into the plasma sheath region, where strong electric fields balance the gravitational force. The resulting systems are vertically compressed and limited by the extent of the sheath. For the investigation of large homogeneous three-dimensional (3D) clouds, an environment with considerably reduced gravity is needed, e.g., a facility on the International Space Station (ISS),^{12–14} or parabolic flights. Once the gravitational force is removed, the weaker electric forces in the bulk plasma are sufficient to confine particles to the plasma bulk region.

In a typical electropositive radio frequency (rf) discharge of a noble gas, the electric field that causes the inward pointing confining force on the particles in turn accelerates the positive ions outward. The ion flow exerts an outward-pointing ion drag force on the particles.^{15,16} This often results in the formation of the so-called void—a region in the discharge center, which is depleted of particles.^{12,17,18} A typical example of a void is shown in Fig. 1(a).

While the physics behind void-formation can be subject of investigations in itself,¹⁹ large homogeneous three-dimensional clouds without the central void are favored to study, e.g., statistical properties of many-particle systems.

It has been shown that the void can be successfully closed by reducing the discharge power, and thus the ion drag force.²⁰ One drawback of this method is that the discharge is operated at powers close to the minimum power needed to maintain it. It can easily terminate, especially in the presence of particles drawing electrons from the discharge onto their surface.

An alternative method to manipulate discharge parameters is the plasma generation by a pulsed power source. A plasma sustained by a pulsed source is in the afterglow during the off-times, i.e., the afterglow is temporal, and it is re-ignited again during the on-time. Global models that describe the evolution of the pulsed plasma can be found in the

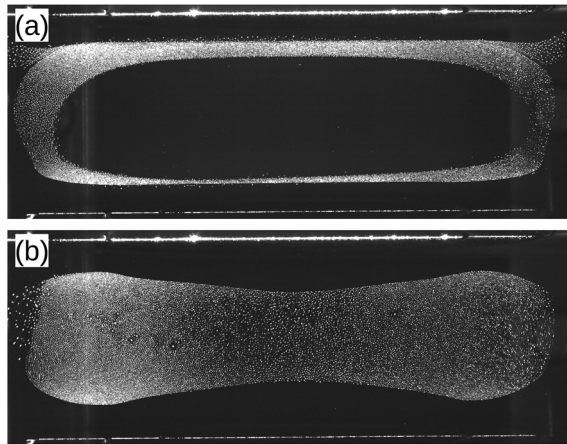


FIG. 1. The images show cross sections through particle systems created in microgravity during a parabolic flight. The particles scatter incident laser light used for illumination (details of the experiment procedure are given in Sec. II). The experimental parameters are: electrode separation 45 mm, neutral gas pressure 20 Pa, and peak-to-peak voltage at the electrode segments 70 V. The particles are melamine-formaldehyde spheres with a diameter of 4.41 μm . (a) Large central void in a continuous radio frequency discharge. (b) No void in a pulsed radio frequency discharge (pulse base period: 200 μs , see Sec. III for details).

literature.^{21–23} Pulsed discharges were, for example, studied as a tool to modify the gas phase chemistry and manipulate ion bombarding energies in the scope of industrial plasma processing,²⁴ or to control the electron energy distribution function.²⁵

During the temporal afterglow, electrons and ions diffuse toward the walls. Dust particles previously charged in the plasma by continuous streams of electrons and ions to their surface lose some of their charge until the charge becomes frozen.²⁶ Since there is no production of electrons and ions, and the electrons are more mobile, the diffusion changes from ambipolar to free, and the remaining charge on dust particles in the discharge is determined by the nature of this transition.^{27,28} The particles themselves can in turn influence the plasma parameters of the decaying plasma by, e.g., emitting previously collected electrons from their surface due to collisions with metastables.^{29,30} Even positive charges have been measured on particles in temporal afterglows,^{31,32} and the effect of the cooling of the background gas in the former plasma region during the off-time on the neutral gas drag experienced by the particles has been studied in a spatiotemporal afterglow.³³ Spatial afterglow, where the afterglow is located in a different region than the region of active plasma production, has further been used to investigate particle decharging.³⁴

Here, we will present a new method for void-closure utilizing a four-channel pulsed rf source and investigate the effects on the particle cloud. The method has the advantage that the average rf power input into the plasma, and thus the plasma density, can be kept constant, while pulse parameters are varied. A series of experiments performed in microgravity during parabolic flights at different neutral gas pressures, discharge volumes and pulse periods demonstrates the effectiveness of the method, even over a wider parameter range. Some basic properties of this “pulsed complex plasma,” such as the spatial particle distribution, and the homogeneity of the particle density are analyzed, and their dependence on the experimental parameters is examined.

The paper is organized as follows. The experimental setup is described in Sec. II, and the experimental procedure and specific parameters for the performed experiments are given in Sec. III. The data analysis methods and respective results are presented in Sec. IV, followed by a discussion of the possible underlying mechanisms for the observed behavior in Sec. V. The paper is concluded in Sec. VI, with an additional outlook for future works.

II. EXPERIMENTAL SETUP

Experiments were performed in the Zyflex plasma chamber.³⁵ The chamber is a cylindrical aluminum vessel with outer diameter of 270 mm and a height of 250 mm. Two segmented electrodes are mounted parallel to each other in the chamber, each consisting of two electrically isolated parts: one central disk-shaped electrode with diameter of 80 mm, surrounded by one ring-shaped electrode with outer diameter of 114 mm as shown in Fig. 2(a). The separation between the segmented electrodes can be adjusted in the range 25 – 75 mm by piezo motors mounted inside the chamber. For a detailed technical description of the chamber, see Ref. 35.

Each of the electrode segments is connected to its own rf channel of a four-channel radio frequency (rf) generator operating at 13.56 MHz. The coupling to the rf is capacitive via a series capacitor of 4.7 nF for each segment. Each two adjacent segments (top or bottom ring and center) were further dc coupled via a coil. The amplitude of each channel, as well as the phases of signals between the channels, can be individually adjusted, while all channels share the same time base. Each channel can be either operated in a continuous mode, or in a pulsed mode as described in detail below. The voltages at the electrode segments were measured by a multi-channel oscilloscope. The oscilloscope made burst measurements of 400 000 samples length with a sampling rate of approximately 80 Ms and 160 ms between the bursts. The burst measurements were evaluated on-the-fly to provide average dc bias voltages V_{dc} for each segment, as explained in more detail in Ref. 35.

After ignition of an argon plasma by applying rf signals to the electrode segments, micrometer-sized particles are injected into the plasma from dispensers mounted in the chamber side walls. The particles are illuminated by a 660 nm diode laser with 60 mW maximum optical output power and beam shaping optics. The optics (Schäfter+Kirchhoff macro line generator) produce a vertically spread, horizontally thin, laser sheet with uniform intensity profile in line direction and an extended range of focus of 82 mm. The laser is mounted such that it illuminates the central vertical cross section of the chamber. The scattered light is recorded by a digital camera with an 8.9 MPixel sensor at a frame rate of 70 frames per second and a spatial resolution of 40 $\mu\text{m}/\text{pixel}$.

For operating in the pulsed mode, an Arduino Nano microcontroller provides trigger signals for each rf channel. The trigger signals are determined by a pre-defined pulse sequence supplied by the user and uploaded to the microcontroller.

A sequence can contain up to 1024 entries (limited by the memory of the microcontroller), describing the on/off states of the four channels at consecutive time steps of the length T_{base} (the base period). The sequence is repeated in an infinite loop. Periodic pulsing, for example, can be achieved by combining short pulses, as illustrated in Fig. 2(b): all four channels are pulsed with a base period of $T_{\text{base}} = 50 \mu\text{s}$, a period of $4T_{\text{base}} = 200 \mu\text{s}$, and a pulse width of

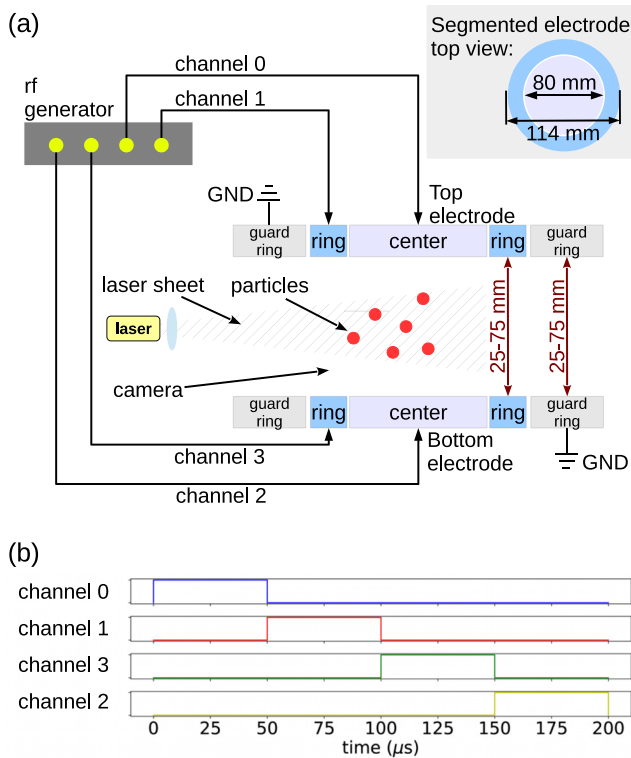


FIG. 2. (a) Schematic of the experimental setup with two segmented electrodes mounted parallel to each other inside the plasma chamber. Each segmented electrode consists of a central disk electrode (light blue) and a ring electrode (dark blue), as illustrated in the inset showing the top view. The electrodes are surrounded by grounded guard rings (gray). Each of the segments is connected to an individually adjustable channel of a four-channel rf generator. Experiments are performed in the following way: A plasma is ignited between the electrodes, micrometer sized particles are injected, and a cross section of the particle system is illuminated by a vertically spread laser sheet. The scattered light is then recorded by cameras. (b) Example of the operation of the four rf channels in a sequential pulsed mode. The on-time of each channel is the time when the shown signals are high. Here, each of the channels is pulsed with a base period of $50 \mu\text{s}$, a period of $200 \mu\text{s}$, and an offset between the channels chosen such that only one channel is on at a time. Repeated infinitely, this type of pulsing would lead to a “circular” switching pattern between the electrodes: top center \rightarrow top ring \rightarrow bottom ring \rightarrow bottom center.

$1T_{\text{base}} = 50 \mu\text{s}$, with an offset of 0, 50, 100, and $150 \mu\text{s}$ for channels 0, 1, 2, 3, respectively. In that example, at each time one channel is on.

Alternatively, a long random sequence can be repeated in a loop to realize, e.g., pseudorandom pulsing of the four channels.

III. EXPERIMENTS

The experimental setup is integrated in racks that can be mounted into an airplane that performs a special flight maneuver (parabola). During a parabola, the forces on the microparticles due to gravity are reduced down to the order of $10^{-2} g$ for $\approx 22 \text{ s}$. Typically, 31 parabolas are flown during one parabolic flight campaign day.

The experiments were conducted as follows: before each parabola, electrode separation, neutral gas pressure, and the voltages applied to the electrodes were adjusted to desired values. Pulsing of the plasma was obtained by consecutive on/off-switching of the four rf channels

in a pseudorandom, pre-calculated sequence. The sequence determines, for each time step in units of the base period T_{base} , one channel to be in the on-state, while all others are switched off. This ensures that at each time, only one rf channel is used to drive the plasma, and that there is no short-term periodic pattern in the succession of channels. Thus, due to the geometric arrangement of the four electrodes, the location of plasma generation is continuously shifted between center (top or bottom) and ring (top or bottom) electrodes in a random fashion. Since one channel is always on, strictly speaking the pulsed plasma does not reach a temporal afterglow state, but rather a spatial and temporal shift of the plasma production region. Therefore, the underlying physics might differ from those in real temporal afterglow. In temporal afterglow, electrons and ions diffuse outward from the former plasma region. In the presented configuration though, a new plasma region is generated immediately after switching off the source of the initial region, and the diffusion of ions and electrons that were generated in the initial region would be under the influence of the (adjacent) region of “newly” generated plasma.

The exact sequence utilized for the experiments is given in the Appendix with additional details on its generation and properties. The only free parameter is T_{base} , which is the minimum time a channel can be in the on-state. Since the length of the sequence is limited by the available memory of the microcontroller, it is continuously repeated from the beginning after completion. This can in principle introduce some kind of long-term periodicity.

At the beginning of each parabola, microparticles (spherical melamine-formaldehyde particles with a diameter of $4.41 \mu\text{m}$) were injected into the plasma and images of the particle distribution were recorded during the 22 s of reduced gravity.

The injection of particles is implemented via the principle of a salt shaker: a reservoir with particles is covered by a sieve. The reservoir is shaken, and particles leave it through the sieve. The amount of injected particles is not clearly defined, since it depends on unknown factors such as the initial location of particle in the reservoir, or the amount of clogging in the sieve holes. Therefore, the particle number can vary between experiment runs, since after each parabola, particles usually drop onto the lower electrode and are lost, and new particles have to be injected in the next run.

The pulse sequence was employed during 13 parabolas for different electrode separations ΔL (45, 75 mm), neutral gas pressures P (5, 20 Pa), peak-to-peak voltages V_{pp} (70, 90 V), and several base periods T_{base} in the range of $50 - 800 \mu\text{s}$. The voltage V_{pp} is adjusted to the same value for each individual electrode segment. Since at each time only one electrode segment is on, V_{pp} is two times the voltage amplitude with respect to ground. The chosen range of T_{base} ensures that the switching between channels happens at frequencies too large for the microparticles to follow: typical dust plasma frequencies for particles with a few micrometer diameter are of the order of $10 - 100 \text{ Hz}$, which is at least one order of magnitude lower than the slowest switching frequency of 1.25 kHz ($T_{\text{base}} = 800 \mu\text{s}$). An oscillation of the particles, or a large-scale motion of the particle cloud through the plasma volume at these high frequencies (which would not be detected by the slower imaging system), can therefore be excluded.

The pulsed mode was either switched on before the start of the microgravity phase, or shortly after particle injection. In two parabolas, T_{base} was changed during the parabola to see the direct effect on the

TABLE I. Experimental parameters for the datasets #1–15: Electrode separation ΔL , neutral gas pressure P , peak-to-peak voltage V_{pp} , average dc bias V_{dc} measured at the top segments with the standard deviation indicating the bias fluctuations, and pulse base period T_{base} .

Dataset #	ΔL (mm)	P (Pa)	V_{pp} (V)	V_{dc} (V)	T_{base} (μ s)
1	75	20	70	-3.1 ± 0.2	50
2	75	20	70	-3.1 ± 0.3	50
3	75	20	70	-3.0 ± 0.4	100
4	75	5	70	-11.5 ± 0.4	50
5	75	5	70	-11.1 ± 0.5	50
6	75	5	70	-11.7 ± 0.6	100
7	45	20	70	-7.5 ± 0.3	50
8	45	20	70	-6.4 ± 1.1	200
9	45	20	70	-5.7 ± 1.9	400
10	45	5	70	-9.9 ± 0.5	50
11	45	5	70	-9.1 ± 0.4	50
12	45	5	70	-9.3 ± 0.7	100
13	45	5	70	-9.0 ± 4.0	800
14	45	5	90	-15.7 ± 0.6	50
15	45	5	90	-15.0 ± 2.6	400

particle cloud at a constant particle number. Therefore, 15 experimental runs with different pulse settings were available for analysis. The experimental parameters are summarized in Table I. The peak-to-peak voltages V_{pp} are those set to the respective driven electrode during the sequence's run, while the dc voltages V_{dc} are given as average over the analyzed data range for the top segments, with the standard deviation indicating the bias fluctuations. The bottom segments deviated from the top segments by a factor of ≈ 0.67 due to differences in the overall series capacitance of the matching circuits. The absolute value of the measured dc bias was lower by factors in the range of 0.12 – 0.51 in the pulsed operation mode compared to a continuous operation (depending on gas pressure and electrode separation).

IV. RESULTS

The first qualitative observation in all performed experiments was that with starting the random pulse mode the central void was instantaneously closed, as shown in Fig. 1(b). This behavior was always reproducible and did in general not depend on neutral gas pressure, rf power, electrode separation, or pulse base period within the tested parameters.

To obtain a more quantitative picture of this observation, the changes in the area accessed by the particles [represented by the two-dimensional (2D) cross section of the cloud] and the particle density and distribution within this area (representing the homogeneity within the cloud) are investigated in more detail. This analysis is performed based on the individual particle coordinates, which are obtained from the recorded images such as Fig. 1 by an intensity weighting method.³⁶

Connected groups of pixels with intensities above a user-chosen threshold are identified as particles, and the particle position is calculated as the intensity weighted center of the pixel group. To improve the results and compensate for possible nonuniformities in the illumination, the threshold was provided by local thresholding with a DOG-filter (difference-of-Gaussian).

A. Cloud area and shape

The cloud shape can be extracted from the particle coordinates as the envelope of the visible cloud. In the two-dimensional cross section provided by the images, the shape represents the area accessed by the particles. It is determined by the balance of forces acting on and between the particles: the electric confinement force pointing from electrodes or grounded walls toward the bulk plasma for the negatively charged particles, and the outward pointing ion drag force and the mutual repulsion between the particles.

The shape of the electric confinement, and thus the cloud shape, depends on the chamber and electrode geometries, which determine the shape and location of the bulk plasma. Since a four-electrode system is used, the plasma geometry can potentially differ from that in a system with two plane-parallel electrodes, especially if the operation is not symmetric as in the case of the random pulsed mode described above.

Figures 3(a) and 3(b) show examples of the cloud shapes of the pulsed complex plasma for two different electrode separations 45 and 75 mm. The envelopes are obtained from single images using the alpha shape method.³⁷ This method can identify shapes, which are not necessarily convex from data given as sets of points, in our case the particle coordinates.

The shape is not necessarily elliptical, and even can become concave with dents at the upper, lower, right, and left sides [see, e.g., Fig. 3(a) for $\Delta L = 75$ mm and $P = 20$ Pa]. At large electrode separation and higher pressure, the vertical cloud extent is larger than at low pressure, presumably due to the larger sheath extent at low pressure. The horizontal extent is not affected. At small electrode separation, the cloud expands horizontally for low pressure, while the vertical extent increases with increasing pressure, but the effect is less pronounced. The total cloud area, shown in Fig. 4(a), has no visible dependence on the pulse parameter T_{base} , or the discharge voltage, and is considerably increased only at large ΔL and high pressure. To quantify the cloud shape, the upper and lower horizontal edges (along x) of the envelopes of 100 consecutive frames at times t of each dataset were fitted by the polynomial $a_c(t)x^2 + b(t)x + c(t)$ with the fit parameter $a_c(t)$ describing the curvature of the edge. Figure 4(b) shows a_c as average over all frames t , and upper and lower edges (choosing the positive sign). All datasets have a positive (negative) curvature at the upper (lower) edge (concave cloud shape), which is stronger pronounced for higher pressures at $\Delta L = 75$ mm and seems to increase with increasing T_{base} for $\Delta L = 45$ mm. In contrast, the shape in the horizontal direction is concave only at $\Delta L = 75$ mm and $P = 20$ Pa, and convex otherwise.

A possible reason for the more distinct concavity in the y -direction could be the proximity of the electrodes: vertically, the particle cloud is confined in the space between the electrodes, and the electric field in the plasma sheath at the electrodes pushes the particles toward the chamber center. In the horizontal direction, the grounded chamber walls are further away, allowing the cloud to expand. Also, the sheath width at the adjacent grounded guard rings should be smaller due to their area being larger than the driven electrode area by a factor of 1.65, not including the chamber walls.

Another quantitative measure of the cloud shape is the eccentricity e . It can be used as a measure for how elliptical the shape is, not taking into account any irregularities such as dents or concave sections.

It is defined as $e = \sqrt{(1 - b_{min}^2/b_{maj}^2)}$ with b_{maj} , b_{min} being the

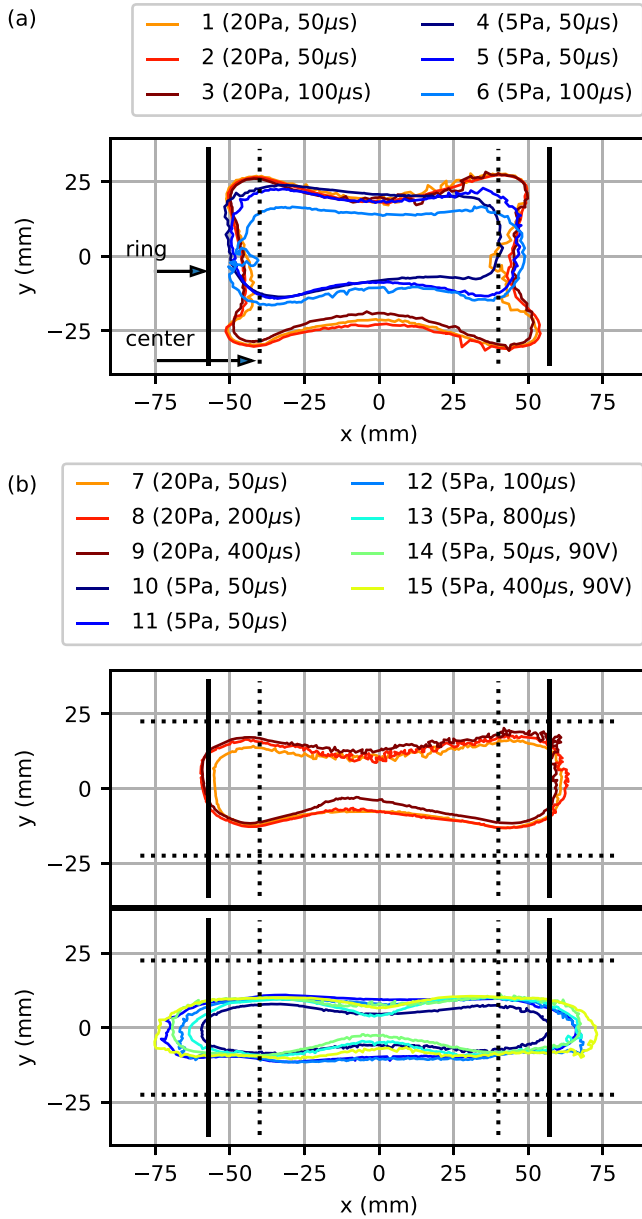


FIG. 3. Cloud shapes obtained from the alpha shape method as explained in the main text, for electrode separations (a) 75 and (b) 45 mm. The numbers in the legends are the dataset numbers defined in Table I. Neutral gas pressure and T_{base} are given in parentheses. V_{pp} was 70 V for all experiments except #14–15. For better visibility, the shapes in (b) are plotted separately for pressures 20 Pa (top) and 5 Pa (bottom). Outer edges of central/ring electrode along x are indicated by vertical solid/dashed lines, and the vertical electrode positions are outside the shown region at ± 37.5 mm (a) and shown as horizontal dashed lines at ± 22.5 mm in (b).

semi-major and semi-minor axes of the ellipse. For a circular cloud, e is 0, and it grows toward 1 as the ellipse becomes more elongated in the vertical direction (defining b_{min} as the semi-minor axis oriented in the vertical direction). The eccentricity was calculated from the eigenvalues of the covariance matrix of the second order central moments

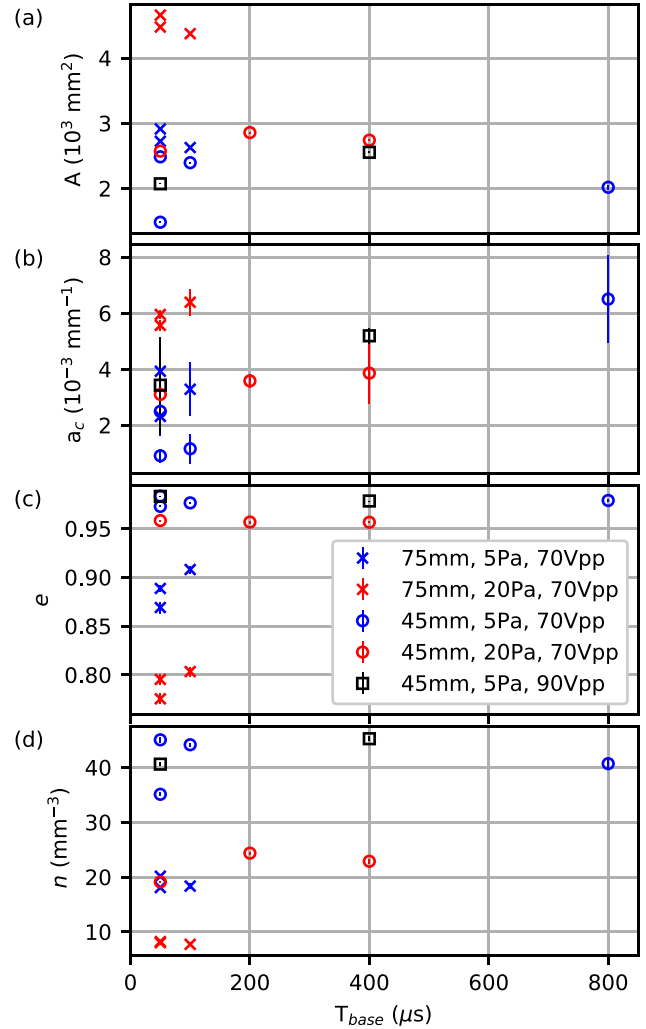


FIG. 4. (a) Area A of the particle cloud, averaged over 100 frames. (b) Curvature a_c of the horizontal cloud edges obtained as the time average of polynomial fits to 100 consecutive frames. (c) Cloud eccentricity e quantifying the elliptic shape of the cloud (in the horizontal direction) with $e = 0$ for a circle, e growing toward 1 for an increasingly elliptic shape. (d) Particle density n from coordinates as described in the main text, averaged over 100 frames. All parameters are plotted vs the pulse base period T_{base} . Error bars for (b) are derived from the uncertainty of the fit parameters, and all other error bars (standard deviation of the mean) are of the size of the plot symbols.

of the image moments³⁸ and is shown in Fig. 4(c). It can be seen that the cloud elongation in the horizontal direction increases with decreasing pressure and decreasing electrode separation, but is does not strongly depend on T_{base} .

As evident from the grouping of data points in Figs. 4(a)–4(c), the two parameters affecting the cloud area and shape strongest are neutral gas pressure and electrode separation. The curvature [Fig. 4(b)] is the only parameter with an additional weak dependence on the pulse parameter T_{base} . The limited amount of data for $\Delta L = 75$ mm at larger T_{base} makes it difficult to draw a clear conclusion, and more experiments need to be performed and analyzed to fill that gap.

B. Particle density

The particle number density determines the dust plasma frequency. The presence of dust can also affect the plasma potential within the cloud, especially for large densities the plasma can be depleted of electrons that are then bound on the particles surface. The density depends not only on the number of injected particles, which can vary between experiment runs due to the technical reasons described in Sec. III, but it is also influenced by the forces acting on the particles, since these determine the accessible area: injecting more particles can result in higher density, but also in cloud expansion if the repulsive force between the particles prevails.

For each time step, the particle density is determined as the number of particles located inside the polygon calculated with the alpha shape method described in Sec. IV A, divided by the polygon area. This gives a time series of densities, which are then averaged over 100 frames to obtain an average density that can be compared between datasets.

Since the recorded images yield particle positions in two dimensions, i.e., representing the number of particles identified in the illuminated two-dimensional (2D) cross section viewed by the camera, the calculated density is a 2D particle density n_{2D} . To convert it to a 3D number density, n_{2D} is divided by the laser width d_l . The laser line shaping optics produce a line with width 0.16 mm in the focus, and 0.22 mm at the edge of the depth of focus, which is located approximately at the outer edge of the electrodes. An average value of $d_l = 0.2$ mm is assumed. This approach is justified by the fact that the particle separations measured in the images are typically larger than the laser width (370 – 885 μm , depending on experimental conditions). Therefore, it is unlikely that more than one particle layer is visible, and the beam shape does not have an impact. The thus obtained density $n = n_{2D}/d_l$ is a representative measure for the 3D particle density and its spatial variations, not the real number density which would require a different optical diagnostic system to measure three-dimensional particle positions in a larger volume.

Figure 4(d) shows n plotted vs T_{base} . As for the cloud area and eccentricity, no correlation with the base period or discharge voltage can be detected, but clearly n decreases with increasing ΔL and pressure.

C. Density gradients

The homogeneity of the density across the cloud is expected to be affected by the shape of the electric potential in the plasma chamber. Regions of higher potential attract the negatively charged particles, but from these regions positive ions are streaming outward. The resulting ion drag force on the particles is pointing outward, counteracting the confining electric forces. If the ion drag force is weak, there might be no visible central void, but still there could be spatial inhomogeneities in the particle density.

The density variations across the particle clouds can be illustrated by density maps obtained from the particle images: the image area is divided into a regular grid with a grid size of 3Δ , with Δ being the average particle separation in a given dataset. The chosen grid size ensures that a grid cell in one image contains on average ten particles. The density of a cell is now calculated as the number of particles in the cell averaged over 100 consecutive frames (keeping the spatial cell location unchanged) and divided by the cell area. Figure 5 shows examples of the density maps for selected electrode separations and pressures.

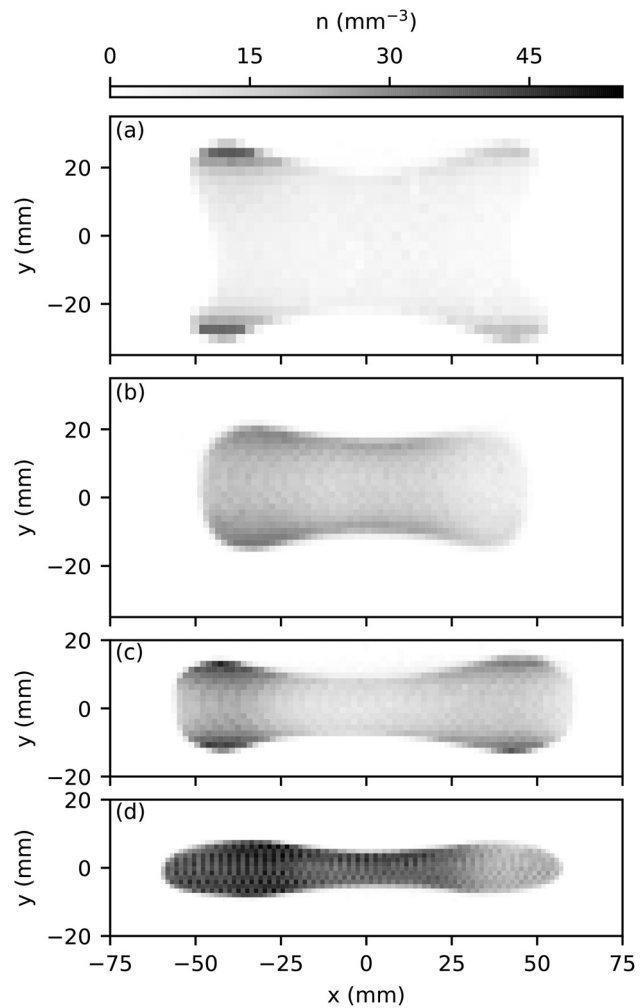


FIG. 5. Density maps for datasets with $T_{\text{base}} = 50 \mu\text{s}$, $V_{\text{pp}} = 70 \text{ V}$ and (a) $\Delta L = 75 \text{ mm}$, $P = 20 \text{ Pa}$ (dataset #1), (b) $\Delta L = 75 \text{ mm}$, $P = 5 \text{ Pa}$ (dataset #5), (c) $\Delta L = 45 \text{ mm}$, $P = 20 \text{ Pa}$ (dataset #7), and (d) $\Delta L = 45 \text{ mm}$, $P = 5 \text{ Pa}$ (dataset #10).

A qualitative observation is that at large $\Delta L = 75 \text{ mm}$, the density is in general higher in the four cloud corners compared to the cloud center. This is most pronounced at high pressure (20 Pa). At 5 Pa, the density is on average higher across the whole cloud, and regions of higher density extend along the top and bottom cloud edges, as visible in Fig. 5(b). A similar picture holds for the smaller electrode separation of 45 mm [Figs. 5(c) and 5(d)], though here the density increase at the cloud corners is accompanied by a general higher density in the outer (left and right) regions at 20 Pa. At 5 Pa, the cloud becomes very dense and the density becomes more uniform across the cloud.

In all examples, the density appears to be lower in the right image half. One factor contributing to this phenomenon is the illumination: the laser illuminating the particles is shining into the chamber from the left image side. At the right side, some of the light is already scattered and the intensity in the laser sheet is therefore reduced, resulting in weaker illumination (thus a reduced particle detection rate and

seemingly reduced n). Another factor could be a small residual acceleration (visible in the acceleration data of the flights) due to the flight maneuver toward the left in the images acting on the particles and increasing the density on that side.

The spatial density gradients can be quantified by calculating horizontal and vertical density profiles: The horizontal density profile is obtained by dividing the particle cloud into vertical slices, or bins. The density in each slice is then obtained as the number of particles in the slice, divided by the slice area. The bin center on the horizontal x -axis is taken as the slice center. The width of the slices is chosen for each dataset to be at least 3Δ (the same as the cell grid size for the density maps). Since the vertical extent of the slices is across the full particle cloud height, which is much larger than the width of the slice, the number of particles in each slice is usually larger than 100. The binning is repeated for the same 100 frames used for the density map calculation in Sec. IV B. To account for temporal drifts of the cloud, for each frame the center position (the average over all particle positions) of the cloud is subtracted. Finally, each slice's density is averaged over the 100 frames.

The same procedure is applied to obtain vertical density profiles, with slices taken along the horizontal direction.

Figures 6(a) and 6(b) show the horizontal and vertical density profiles for $\Delta L = 75$ and 45 mm, respectively. In the horizontal profiles [left images in Figs. 6(a) and 6(b)], a decrease in density in the

positive x -direction can be seen, which is due to the lower particle detection rate in the right half of the images as explained above.

The horizontal profiles at $\Delta L = 75$ mm [Fig. 6(a), left] at $P = 5$ Pa exhibit a double peak structure with the two maxima located within the central electrode confines (datasets #4–6), and a parabolic shape between the peaks. The minimum is located near the chamber center with a slight offset, presumably caused by residual forces during the flight maneuver. At 20 Pa (datasets #1–3), the density is in general lower, and there are no peaks but an increase in density toward the electrode edge. The perceived flatness of the profiles in the central region especially for positive x is misleading, since there the particle detection rate was low. The pronounced density increase toward the edges is caused by the high density in the cloud corners, visible as dark areas in Fig. 5(a), which considerably increase the density of the outermost slices. The vertical profiles [Fig. 6(a), right] exhibit a parabolic shape in the central region, indicating a parabolic potential gradient between the electrodes positioned at $y = \pm 37.5$ mm. This indicates that regardless of the random pulsing of the four channels and their geometric configuration, the bulk plasma is—on time average—located in the central volume of the chamber. As for the horizontal profiles, the vertical profiles are flatter at higher pressure (omitting the outer edges where the statistic is expected to be poor), while the overall density is larger for the lower pressure.

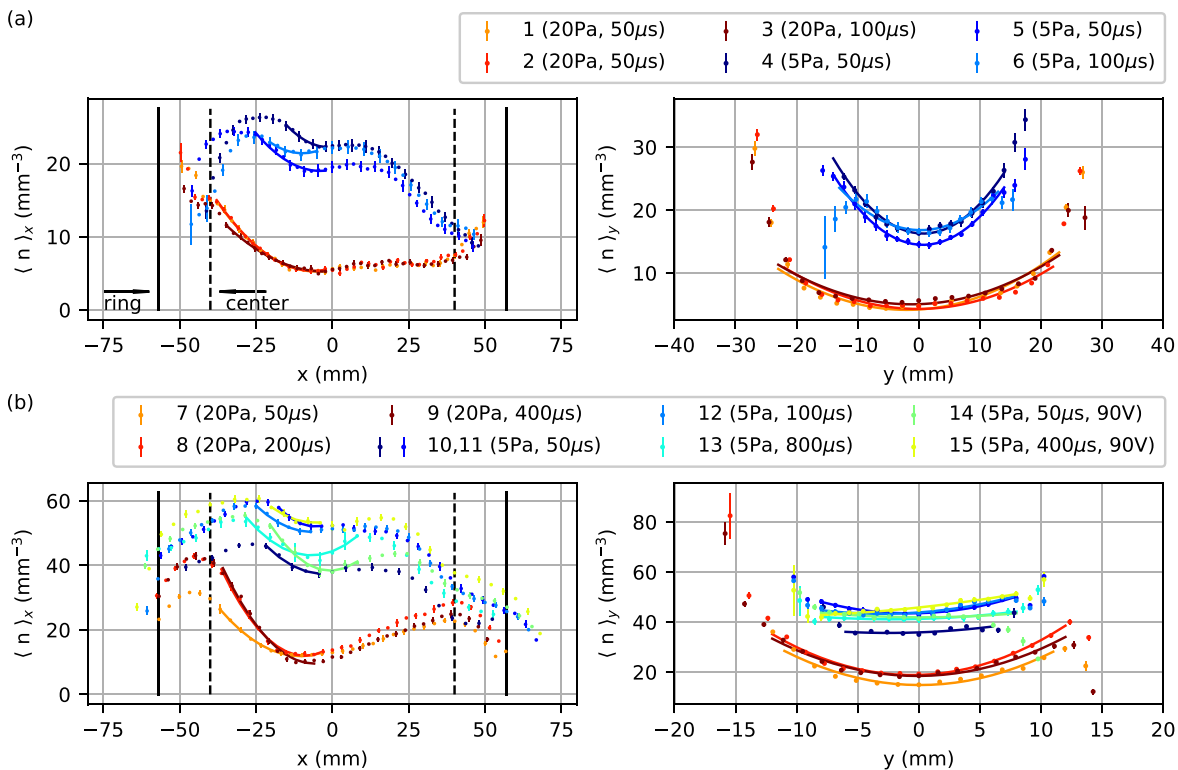


FIG. 6. Density profiles (colored dots) for (a) $\Delta L = 75$ and (b) $\Delta L = 45$ mm. The left (right) column shows the profile along x (y). Error bars are standard deviations from averaging over 100 frames. The numbers in the legends are the dataset numbers defined in Table I, and neutral gas pressure and pulse base period are additionally given in parentheses. The position of the central and ring electrode outer edges is indicated by vertical solid and dashed black lines in the x profiles (left images). The top and bottom electrode positions in the vertical profiles (right images) are at $y = \pm 37.5$ and $y = \pm 22.5$ mm (b), respectively. The fitted quadratic functions are shown as solid lines with colors corresponding to the dataset color.

At $\Delta L = 45$ mm [Fig. 6(b)], the double peak structure in the horizontal profiles (left image) appears also for the high pressure case (datasets #7–9), with the two maxima located within or at the edge of the central electrode. Again, the density is higher for 5 Pa (datasets #11–15). The vertical profiles (right image) are parabolic at 20 Pa with a lower density, and they become comparably flat at low pressure. The electrodes are located at $y = \pm 22.5$ mm in the right image.

Comparing the two sets at different ΔL , it is obvious that the density for the smaller ΔL is approximately twice as large along the profiles, in agreement with the averaged density n [Fig. 4(d)].

Horizontal (x) and vertical (y) profiles were fitted by quadratic functions $a_\xi \xi^2 + b_\xi \xi + c_\xi$ with $\xi = x, y$, respectively. The fit parameters a_ξ , b_ξ , and c_ξ describe the curvature, the displacement, and the vertical offset. The fits are shown as solid lines in Fig. 6. Due to the decrease in density in the positive x -direction, the fit to the horizontal profiles was performed only in the left part of the profiles, where the parabolic shape was still clearly visible. The left cutoff was chosen either as the position of the maximum density value, or at the edge of the center electrode indicated by the dashed line if no local maximum was detectable.

For the vertical profiles, the data range for the fit was chosen such that the best agreement was in the central region, omitting the edges if necessary. The homogeneity in the central region, where edge effects have less influence on the particle dynamics, is in general of larger interest for scientific studies.

The fit parameters a_x and a_y as a measure for the curvatures are presented in Fig. 7 plotted vs T_{base} , yielding a quantitative comparison of the homogeneity of the clouds at different experimental parameters.

The curvature of the horizontal profiles [Fig. 7(a)] is generally larger for $\Delta L = 45$ mm, with no clear correlation to gas pressure, discharge voltage, or T_{base} . For $\Delta L = 75$ mm, the curvature is slightly larger at lower pressures. The vertical curvature [Fig. 7(b)] exhibits similar behavior, though here the curvature for $\Delta L = 45$ mm increases with pressure, while it decreases with P for $\Delta L = 75$ mm. A distinct trend of either horizontal or vertical curvature with T_{base} cannot be detected. As already mentioned before, more experimental data at different pulse periods are needed, and corresponding experiments are already scheduled, especially for the large electrode separation.

Figures 7(c) and 7(d) show the horizontal and vertical curvatures vs the particle density n . It becomes evident that a_x and a_y are grouped at specific n according to neutral gas pressure and electrode separation, with no dependence on the discharge voltage V_{pp} .

V. DISCUSSION

The presented results indicate that the parameters with the largest influence on the particle cloud are neutral gas pressure P and electrode separation ΔL , with a weak influence of pulse base period T_{base} on the cloud shape. The observed dependencies and possible explanations are discussed in the following.

From the particle and energy balance for electropositive plasmas follows that increasing the neutral gas pressure decreases the electron temperature T_e and increases the plasma density n_0 .²²

The effect of changing the electrode separation is more difficult to interpret. According to the self-consistent equations for the inhomogeneous discharge model for a cylindrical capacitively coupled rf discharge with plane-parallel electrodes,²² if the sheath voltage is held constant, the plasma density can increase if the electrode separation is increased. The reason lies in the increase in the electric potential across the discharge in the axial direction for increased discharge length

(implying a larger power input into the plasma). This also affects the electron temperature (though not as pronounced as the influence of gas pressure): T_e decreases with increasing electrode separation. It still needs to be investigated if this model is applicable to the geometrical configuration of the four-electrode system of the Zyflex chamber, and the (asymmetric) operation of the four electrode segments in the described pulsed mode, but it can at least give an indication of the expected influence on the plasma parameters.

In summary, T_e decreases with increasing P and ΔL , and n_0 increases with P and ΔL .

That implies that, for large ΔL and P (low T_e , high n_0) the particle charges Q_p become lower (since they depend on the mobility of electrons) and at the same time more ions are available that can induce a drag force on the particles. While the directed part of the ion drag force scales linearly with the ion density, the Coulomb part scales linearly with the ion density, and with the squared particle potential Q_p^2 . The two effects (decreased Q_p , increased ion flow) can cancel out if the parameters are suitable and all other effects are ignored (e.g., change of particle charging due to streaming ions and change of ion velocity with pressure), and are therefore difficult to interpret without further data, e.g., from plasma simulations.

The pressure dependance of T_e is well established and yields an decrease in the Debye length and sheath width with increasing P . The bulk plasma volume increases, and the visible particle cloud area A (representing the accessible volume as its 2D projection) increases. The effect is distinct for $\Delta L = 75$ mm, but less pronounced for $\Delta L = 45$ mm [Fig. 4(a)]. Here, the larger areas at $\Delta L = 75$ mm are due to the generally increased plasma volume.

The concave cloud shape [Fig. 4(b)] implies an inward pointing force from the electrodes toward the chamber center. A possible reason is the effect of the pulsed operation of the four channels on the ion flow: on a time average, the ion flow direction could be manipulated such that it is pointing not from the chamber center outward, but from a region close to the central electrode toward the adjacent ring electrode with both radial and axial components (on top and bottom chamber sides, respectively). The ion drag force would then push the particles away from the central electrodes with a force component pointing toward the chamber center. This could explain not only the absence of the central void, but also a stronger curvature at higher pressures and ΔL if the ion drag force increases at these conditions. The latter implies an increase in the ion flow $n_0 u_i$ with the ion drift velocity u_i (e.g., higher n_0 , larger ion flow, and stronger ion drag force). This assumption has to be examined further with the help of plasma simulations in a next step. The increase in the curvature with increasing T_{base} might also indicate a further increase in the average ion drag force from the electrodes toward the bulk, caused by the longer time the directed ion flow acts on the particle cloud, as the frequency of switching between the channels comes closer to the dust plasma frequency (1.25 kHz at $T_{\text{base}} = 800$ μs).

The eccentricity e [Fig. 4(c)] is larger for lower P , meaning an increasingly elliptic shape. Here, the sheath width becomes larger and the particle cloud is presumably more compressed in the vertical direction between the electrodes, yielding an increase in the horizontal direction (i.e., the cloud is squeezed between the electrode sheaths). The measurements at lower ΔL yield a larger e , which could be due to the additional dependance of T_e on ΔL (increase in T_e , increase in sheath width, more compression).

The increase in the particle density n [Fig. 4(d)] with decreasing P can also be attributed to the stronger compression between the sheaths. The decrease in n for larger ΔL is contrary to the above-mentioned arguments, though. An explanation could be as follows: assuming that the injected number of particles is at least approximately of the same order of magnitude (the number of shakes of the particle dispenser was the same), the density is expected to decrease in that cases since fewer particles are available to fill a larger area, respectively, volume, at large ΔL . The interpretation of the dependence of n on the experimental parameters is therefore rather speculative without further measurements, especially without the ability to control the amount of injected particles more precisely. Figure 4(d) gives a qualitative comparison of the experiment runs with regard to the particle density, though.

The curvatures of the density profiles can best be interpreted by the results presented in Figs. 7(c) and 7(d). The dependences of a_x and a_y on P and ΔL are in agreement with the dependence of n on P and ΔL [Fig. 4(d)]. The increase in a_y with P at $\Delta L = 45$ mm is further in agreement with the observation that the curvature of the cloud envelope in the horizontal direction, a_c , increases with increasing pressure [Fig. 4(b)]: the increase in a_c with pressure indicates a stronger cloud compression in the vertical direction, especially in the (horizontally) central cloud region, which in turn causes a stronger density gradient.

The reversion of pressure dependence at large electrode separation can be explained by the same argument as presented above for the density: At the largest ΔL not enough particles were injected to fill the available volume and thus the results might be misleading.

The vertical density gradients are generally larger than the horizontal gradients (a_y is nearly one magnitude larger than a_x). Again, this can be explained by the stronger potential gradients and thus confinement forces between the driven electrodes, compared to the confinement in the horizontal direction that mainly depends on the potential difference between plasma and grounded surfaces (guard ring, chamber walls).

The above-mentioned discussion gives rather qualitative explanations of the observed phenomena based on general plasma models. In the following paragraphs, possible mechanisms that could be responsible for void closure are discussed in more detail. The results of particle-in-cell (PIC) simulations at comparable conditions give a more quantitative picture of the expected background plasma parameters: The simulations were performed for the Zylflex chamber with a continuous rf voltage of 40 V peak-to-peak applied to all segments, and a phase shift of 180° between top and bottom segments (push/pull mode).³⁵ The voltage amplitude between facing segments was therefore 40 V, comparable to the 35 V amplitude between segments in the pulsed mode with only one segment being active at a time. Though the plasma parameters were estimated for a continuous mode, the pulsed operation mode applied in the experiments also provides an active plasma sustainment at all times, with reduced driven electrode area compared to the simulations. As can be seen from estimations based on the inhomogeneous discharge model,²² a change of electrode area does not have a strong impact on n_0 and T_e ; thus, they seem appropriate as a first estimate. The simulations yield plasma density and electron temperature for $\Delta L = 75$, with $T_e = 2.3$ (2.0) eV and $n_0 = 2.4 \times 10^{14}$ (3.7×10^{14}) m^{-3} for $P = 5$ (20) Pa. From these parameters, the ratio of ion drag to electric force can be estimated following the approach in Ref. 20 for subthermal ions in the bulk

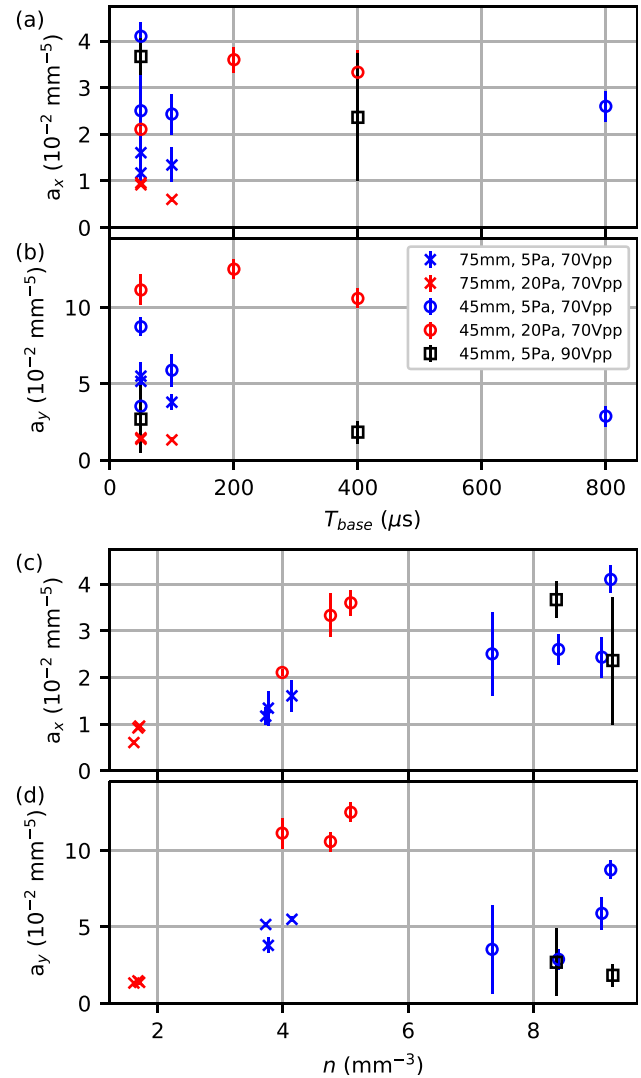


FIG. 7. Fit parameters a_x (a) and a_y (b) vs pulse base period T_{base} . The parameters represent the curvature of the density profiles in the horizontal and vertical direction and were obtained by a quadratic fits to the density profiles as described in the main text. (c) and (d) a_x and a_y vs particle density n .

discharge, yielding $F_i/F_e = 2.03$ (0.64) for $P = 5$ (20) Pa. This would mean that at 20 Pa, there should be no central void, while at 5 Pa, to achieve a void-closure, the ion density would need to be reduced by a factor of 3. The simulations yield similar results for a smaller $\Delta L = 50$ mm. While the void closure at 20 Pa could therefore in principle be explained by a ratio $F_i/F_e < 1$, it cannot explain the void-free system that was observed also at 5 Pa.

The influence of the dc bias persisting on the electrodes should also play no significant role: an inspection of the (non-averaged) dc bias trend within the burst measurements of 400 000 samples length showed that the dc bias does not go to zero on non-active segments for fast switching (50, 100 μs), but stays around its average (negative) value, shown in Table I. For slower switching, the bias magnitude

decreases toward zero on time scales of 0.3 – 1 ms if a segment or its neighboring segment is not driven. While a strong negative bias could aid to cloud compression and void closure as reported previously,¹³ the relatively small magnitude of the bias in pulsed mode would rather impede the observed behavior.

Regarding the effects of afterglow, in a real temporal afterglow (all channels pulsed simultaneously) one would expect a reduced electron temperature and plasma density on a time average. By this, particle charges would be reduced, and the forces on particles would be affected due to the reduced ion flow and electric fields. In spatial afterglow, particles would reside in a region of plasma diffusion, with the particle charge depending on the local characteristic diffusion length. In the presented experiments, the active plasma region is shifted within the chamber, which means that at any time, plasma is being sustained by a driven electrode. The shifting happens at time scales of the order of typical time scales of density decay in temporal afterglow (tens of microseconds up to milliseconds),²⁸ which would result in a combination of temporal and spatial afterglow, the effect of which on the plasma parameters and particle charges needs further evaluation. It could be expected that ion flow from a former active plasma region will still be present, but it would be affected by the flow emerging from the new active plasma region. If that leads, on a time average, to a stronger ion flow toward the geometrical chamber center, this would favor closure of the central void in a particle cloud.

The manipulation of the direction of the ion flow, not necessarily its magnitude, could actually provide an explanation of the observed void closure: typically, ions stream outward from the bulk plasma toward the walls due to the ambipolar field. If the topology of the discharge is changed to, e.g., a torus surrounding the central region, the ion flow direction can be inverted as observed previously.³⁹ The fast shifting of the active plasma region could be the cause for such a topology change: the active plasma region is shifted between areas close to either top or bottom ring and center electrodes and is never located in the chamber center (as would be the case for a continuously driven symmetric push–pull mode). On a time average, this could lead to a discharge geometry that acts as an ion source from a toroidal outer region toward the geometric chamber center. The direction of the ion drag force on the particles would be modified such that it points toward the chamber center and pushes particles into the center (provided that the electric force is weak), thus closing the central void. This assumption and the nature of the spatiotemporal afterglow need verification by experiments and simulations that are subject to future work.

VI. CONCLUSION AND OUTLOOK

A new technique for closing the, often unwanted, central void in a cloud of micrometer-sized particles immersed in the bulk of a low-temperature plasma in microgravity has been presented. The technique involves the utilization of a four-channel rf generator, connected to four separate electrodes in the plasma chamber, that is operated in a pulsed mode: each of the channels is pulsed by applying a random sequence of on- and off-times. The sequences are chosen such that at each time period T_{base} , only one channel (one electrode) is in the “on” state (random pulsing). The random sequence (given in the [Appendix](#)) was chosen to omit potential effects due to short-term periodicity.

First observations of 15 experimental runs performed during a parabolic flight campaign at different discharge conditions show that void closure appears independent of the parameters neutral gas

pressure, discharge power, or discharge volume, as long as the rf generator was operated in the pulsed mode.

The characteristics of the particle system for different experimental parameters were investigated qualitatively and quantitatively by analyzing properties of the shape of the particle cloud (area, edge curvature, and eccentricity), and the particle density and density gradients. While the pulse sequence was not changed in this first set of experiments, the pulse base period T_{base} was modified to investigate the influence of this pulse parameter on the particles. The results show that there is no distinct indication that the investigated particle cloud characteristics depend on T_{base} within the tested parameter range. A weak dependence of the cloud curvature on T_{base} could indicate an influence on the magnitude of the ion flow and thus the ion drag force. This observation requires further investigations of the underlying plasma processes, which will also help to uncover the reasons for void-closure that are presumed to be connected to the direction of the ion flow in the special conditions of the pulsed operation mode.

It was found that neutral gas pressure and electrode separation (plasma volume or discharge geometry) have the strongest influence, with larger electrode separation yielding larger and more homogeneous particle clouds, while larger pressures seem to cause larger density gradients in the vertical direction—the later being an observation that needs more experimental data to be confirmed.

The minor influence of T_{base} is an interesting result since it implies that the pulsed mode does not introduce new physical effects on the particles aside from the void closure, thus allowing to perform studies of fundamental processes in extended dust systems without the need to adapt the existing theoretical models to include specific effects of the pulsed mode.

Even though the density of the particle cloud, as analyzed in [Sec. IV C](#), is not perfectly uniform and shows gradients depending on gas pressure and electrode separation, the void-free system provides access to large (3D) particle clouds without inner boundaries. Tuning of the experimental conditions could further improve the homogeneity, e.g., using larger electrode separations.

The proposed technique shows great potential for application in experiments dedicated to fundamental studies of complex plasma, for example, in the future complex plasma facility COMPACT⁴⁰ that is currently under development, and is intended to be operated onboard an orbital platform, e.g., the International Space Station (ISS).

As evident from the presented data, a larger amount of datasets is needed to expand the parameter space and get a deeper understanding of the underlying processes, especially the physical reason for void closure. A detailed experimental program, to be conducted on parabolic flights, has been worked out to investigate the influence of, e.g., periodic sequences, the necessity of a four electrode system, and a wider range of base periods at different gas pressures, discharge voltages, and volumes. In addition, plasma simulations are needed to shed light on the modification of plasma parameters during the pulsed operation. The simulations can yield plasma density and electron temperature, but also the spatial ion flow pattern and electric fields in the chamber that will give further insight into the mechanism of the void closure.

ACKNOWLEDGMENTS

This work and the authors were funded by DLR/BMWi (Nos. FKZ 50WP0700 and FKZ 50WM1441) and the Bavarian Ministry of Economic Affairs and Media, Energy and Technology (StMWi).

C. A. Knappek and D. P. Mohr are currently funded by DLR/BMWi FKZ 50WM2161. We thank H. M. Thomas for carefully reading the manuscript.

AUTHOR DECLARATIONS

Conflict of Interest

The authors have no conflicts to disclose.

Author Contributions

C. A. Knappek: Formal analysis (lead); Investigation (equal); Project administration (lead); Validation (equal); Visualization (lead); Writing – original draft (lead); Writing – review & editing (lead). **D. P. Mohr:** Data curation (lead); Formal analysis (supporting); Investigation (equal); Software (lead); Validation (equal); Writing – review & editing (supporting). **P. Huber:** Data curation (supporting); Investigation (equal); Software (supporting); Validation (supporting).

DATA AVAILABILITY

The data that support the findings of this study are available from the corresponding author upon reasonable request.

APPENDIX: PSEUDORANDOM SEQUENCE

The sequence was generated with Python and the NumPy package in the following way: at first, a list of length 1024 was generated, with equal occurrence of the numbers 0, 1, 2, and 3, i.e., 256 occurrences of each element. The numbers represent the channels of the rf generator, connected to the electrode segments, as indicated in Fig. 2: top center (0), top ring (1), bottom center (2), and bottom ring (3).

Then, the list was shuffled using the function `numpy.random.shuffle`, which is based on the Mersenne Twister.⁴¹ The result was a list of pseudorandomly distributed numbers 0, 1, 2, and 3. During the presented experiments, accidentally only the first 256 entries of the list were used, which are as follows:

```
0113001021302210103301132010311303010301232202101100
0212122112210112232223330233023112211030321022000211131
32223122112123100331013003300211022332122221221112130223
23312212101213330022302013131210201020310120132022021232
3210100221000301013312032103330330200.
```

Each number in the list represents a time interval of the length of the base period T_{base} . The respective number determines which channel is in the on-state at this time interval, i.e., 0 means channel 0 is on. The list is converted into a sequence of bytes, each byte containing the state of all four channels for one specific time step, with a true bit describing the on-state of a channel. This sequence was loaded into the memory of an Arduino Nano microcontroller, which triggered the four channels of the rf generator via four digital signal outputs (high or low for on- or off-states, respectively) on one register (resulting in simultaneous switching), with the base period T_{base} as the free parameter.

To illustrate the uniformity of the sequences, Fig. 8 shows the frequency spectra obtained from a Fast Fourier Transform of each channel's occurrence in the shortened list of length 256, as a basic statistical test for a random sequence exhibiting pseudorandom noise over all detectable frequencies.

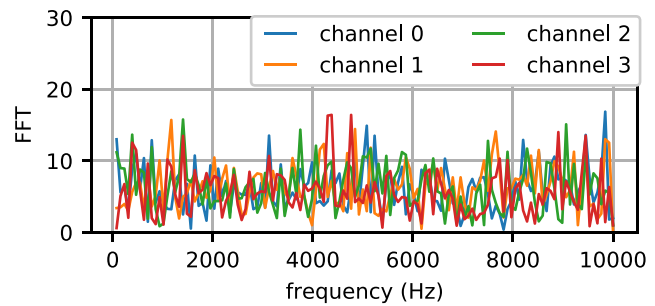


FIG. 8. Fast Fourier transform of each channel's occurrence (list of on- and off-states for each channel).

REFERENCES

- G. E. Morfill and A. V. Ivlev, "Complex plasmas: An interdisciplinary research field," *Rev. Mod. Phys.* **81**, 1353–1404 (2009).
- V. Fortov, A. Ivlev, S. Khrapak, A. Khrapak, and G. Morfill, "Complex (dusty) plasmas: Current status, open issues, perspectives," *Phys. Rep.* **421**, 1–103 (2005).
- A. Piel, "Plasma crystals: Experiments and simulation," *Plasma Phys. Controlled Fusion* **59**, 014001 (2017).
- A. Melzer, *Physics of Dusty Plasmas: An Introduction* (Springer Nature, Cham, Switzerland, 2019).
- M. Rubin-Zuzic, G. E. Morfill, A. V. Ivlev, R. Pompl, B. A. Klumov, W. Bunk, H. M. Thomas, H. Rothermel, O. Havnes, and A. Fouquet, "Kinetic development of crystallization fronts in complex plasmas," *Nat. Phys.* **2**, 181–185 (2006).
- C. A. Knappek, D. Samsonov, S. Zhdanov, U. Konopka, and G. E. Morfill, "Recrystallization of a 2D plasma crystal," *Phys. Rev. Lett.* **98**, 015004 (2007).
- W. Sun, M. Schwabe, H. M. Thomas, A. M. Lipaev, V. I. Molotkov, V. E. Fortov, Y. Feng, Y.-F. Lin, J. Zhang, Y. Guo, and C.-R. Du, "Dissipative solitary wave at the interface of a binary complex plasma," *Europhys. Lett.* **122**, 55001 (2018).
- Y.-Y. Tsai, J.-Y. Tsai, and L. I, "Generation of acoustic rogue waves in dusty plasmas through three-dimensional particle focusing by distorted waveforms," *Nat. Phys.* **12**, 573–577 (2016).
- A. Kananovich and J. Goree, "Shocks propagate in a 2D dusty plasma with less attenuation than due to gas friction alone," *Phys. Plasmas* **27**, 113704 (2020).
- M. Schwabe, S. Zhdanov, and C. R ath, "Instability onset and scaling laws of an auto-oscillating turbulent flow in a complex plasma," *Phys. Rev. E* **95**, 041201 (2017).
- P.-C. Lin, W.-J. Chen, and L. I, "Percolating transition to acoustic wave turbulence in dusty plasmas," *Phys. Plasmas* **27**, 010703 (2020).
- A. P. Nefedov, G. E. Morfill, V. E. Fortov, H. M. Thomas, H. Rothermel, T. Hagl, A. V. Ivlev, M. Zuzic, B. A. Klumov, A. M. Lipaev, V. I. Molotkov, O. F. Petrov, Y. P. Gidzenko, S. K. Krikalev, W. Shepherd, A. I. Ivanov, M. Roth, H. Binnenbruck, J. A. Goree, and Y. P. Semenov, "PKE-Nefedov*: plasma crystal experiments on the international space station," *New J. Phys.* **5**, 33 (2003).
- H. M. Thomas, G. E. Morfill, V. E. Fortov, A. V. Ivlev, V. I. Molotkov, A. M. Lipaev, T. Hagl, H. Rothermel, S. A. Khrapak, R. K. Suetterlin, M. Rubin-Zuzic, O. F. Petrov, V. I. Tokarev, and S. K. Krikalev, "Complex plasma laboratory PK-3 plus on the international space station," *New J. Phys.* **10**, 033036 (2008).
- M. Y. Pustyl'nik, M. A. Fink, V. Nosenko, T. Shtanova, T. Hagl, H. M. Thomas, A. V. Zobnin, A. M. Lipaev, A. D. Usachev, V. I. Molotkov, O. F. Petrov, V. E. Fortov, C. Rau, C. Deysenroth, S. Albrecht, M. Kretschmer, M. H. Thoma, G. E. Morfill, R. Seurig, A. Stettner, V. A. Alyamovskaya, A. Orr, E. Kufner, E. G. Lavrenko, G. I. Padalka, E. O. Serova, A. M. Samokutayev, and S. Christoforetti, "Plasmakristall-4: New complex (dusty) plasma laboratory on board the international space station," *Rev. Sci. Instrum.* **87**, 093505 (2016).
- S. A. Khrapak, A. V. Ivlev, S. K. Zhdanov, and G. E. Morfill, "Hybrid approach to the ion drag force," *Phys. Plasmas* **12**, 042308 (2005).

- ¹⁶I. H. Hutchinson, "Collisionless ion drag force on a spherical grain," *Plasma Phys. Controlled Fusion* **48**, 185 (2006).
- ¹⁷G. E. Morfill, H. M. Thomas, U. Konopka, H. Rothermel, M. Zuzic, A. Ivlev, and J. Goree, "Condensed plasmas under microgravity," *Phys. Rev. Lett.* **83**, 1598–1601 (1999).
- ¹⁸J. Goree, G. E. Morfill, V. N. Tsytovich, and S. V. Vladimirov, "Theory of dust voids in plasmas," *Phys. Rev. E* **59**, 7055–7067 (1999).
- ¹⁹M. Y. Pustynnik, I. L. Semenov, E. Zähringer, and H. M. Thomas, "Capacitively coupled rf discharge with a large amount of microparticles: Spatiotemporal emission pattern and microparticle arrangement," *Phys. Rev. E* **96**, 033203 (2017).
- ²⁰A. M. Lipaev, S. A. Khrapak, V. I. Molotkov, G. E. Morfill, V. E. Fortov, A. V. Ivlev, H. M. Thomas, A. G. Khrapak, V. N. Naumkin, A. I. Ivanov, S. E. Tretschke, and G. I. Padalka, "Void closure in complex plasmas under microgravity conditions," *Phys. Rev. Lett.* **98**, 265006 (2007).
- ²¹M. A. Lieberman and S. Ashida, "Global models of pulse-power-modulated high-density, low-pressure discharges," *Plasma Sources Sci. Technol.* **5**, 145 (1996).
- ²²M. Lieberman and A. Lichtenberg, *Principles of Plasma Discharges and Materials Processing* (Wiley, 2005).
- ²³F.-X. Liu, X.-M. Guo, and Y.-K. Pu, "Electron cooling and plasma density decay in early afterglow of low pressure argon plasmas," *Plasma Sources Sci. Technol.* **24**, 034013 (2015).
- ²⁴J. P. Booth, G. Cunge, N. Sadeghi, and R. W. Boswell, "The transition from symmetric to asymmetric discharges in pulsed 13.56 MHz capacitively coupled plasmas," *J. Appl. Phys.* **82**, 552–560 (1997).
- ²⁵S.-H. Song and M. J. Kushner, "Control of electron energy distributions and plasma characteristics of dual frequency, pulsed capacitively coupled plasmas sustained in Ar and Ar/CF₄/O₂," *Plasma Sources Sci. Technol.* **21**, 055028 (2012).
- ²⁶A. Ivlev, M. Kretschmer, M. Zuzic, G. Morfill, H. Rothermel, H. Thomas, V. Fortov, V. Molotkov, A. Nefedov, A. Lipaev, O. Petrov, Y. Baturin, A. Ivanov, and J. Goree, "Decharging of complex plasmas: First kinetic observations," *Phys. Rev. Lett.* **90**, 055003 (2003).
- ²⁷L. Couëdel, A. A. Samarian, M. Mikikian, and L. Boufendi, "Influence of the ambipolar-to-free diffusion transition on dust particle charge in a complex plasma afterglow," *Phys. Plasmas* **15**, 063705 (2008).
- ²⁸L. Couëdel, "Temporal dusty plasma afterglow: A review," *Front. Phys.* **10**, 1015603 (2022).
- ²⁹I. B. Denysenko, I. Stefanović, M. Mikikian, E. Kovacevic, and J. Berndt, "Argon/dust and pure argon pulsed plasmas explored using a spatially-averaged model," *J. Phys. D* **54**, 065202 (2021).
- ³⁰I. B. Denysenko, M. Mikikian, and N. A. Azarenkov, "Dust dynamics during the plasma afterglow," *J. Phys. D* **55**, 095201 (2022).
- ³¹N. Chaubey, J. Goree, S. J. Lanham, and M. J. Kushner, "Positive charging of grains in an afterglow plasma is enhanced by ions drifting in an electric field," *Phys. Plasmas* **28**, 103702 (2021).
- ³²N. Chaubey and J. Goree, "Coulomb expansion of a thin dust cloud observed experimentally under afterglow plasma conditions," *Phys. Plasmas* **29**, 113705 (2022).
- ³³J. C. A. van Huijstee, P. Blom, A. T. A. Peijnenburg, and J. Beckers, "Spatio-temporal plasma afterglow induces additional neutral drag force on microparticles," *Front. Phys.* **10**, 926160 (2022).
- ³⁴B. van Minderhout, J. C. A. van Huijstee, A. T. A. Peijnenburg, P. Blom, G. M. W. Kroesen, and J. Beckers, "Charge neutralisation of microparticles by pulsing a low-pressure shielded spatial plasma afterglow," *Plasma Sources Sci. Technol.* **30**, 045016 (2021).
- ³⁵C. A. Knapek, U. Konopka, D. P. Mohr, P. Huber, A. M. Lipaev, and H. M. Thomas, "Zyflex: Next generation plasma chamber for complex plasma research in space," *Rev. Sci. Instrum.* **92**, 103505 (2021).
- ³⁶D. P. Mohr, C. A. Knapek, P. Huber, and E. Zaehring, "Algorithms for particle detection in complex plasmas," *J. Imaging* **5**, 30 (2019).
- ³⁷H. Edelsbrunner, D. Kirkpatrick, and R. Seidel, "On the shape of a set of points in the plane," *IEEE Trans. Inf. Theory* **29**, 551–559 (1983).
- ³⁸J. Flusser, T. Suk, and B. Zitová, *2D and 3D Image Analysis by Moments* (John Wiley & Sons, Ltd, 2016), pp. 1–529.
- ³⁹C. Schmidt, O. Arp, and A. Piel, "Spatially extended void-free dusty plasmas in a laboratory radio-frequency discharge," *Phys. Plasmas* **18**, 013704 (2011).
- ⁴⁰C. A. Knapek, L. Couédel, A. Dove, J. Goree, U. Konopka, A. Melzer, S. Ratynskaia, M. H. Thoma, and H. M. Thomas, "COMPACT—A new complex plasma facility for the ISS," *Plasma Phys. Controlled Fusion* **64**, 124006 (2022).
- ⁴¹M. Matsumoto and T. Nishimura, "Mersenne twister: A 623-dimensionally equidistributed uniform pseudo-random number generator," *ACM Trans. Model. Comput. Simul.* **8**, 3–30 (1998).